Acta Astronautica 201 (2022) 83–93

Contents lists available at ScienceDirect

Acta Astronautica

journal homepage: www.elsevier.com/locate/actaastro

Robust disturbance observer-based fast maneuver method for attitude control of optical remote sensing satellites

Youyang Qu [a,b,c], Xing Zhong [a,b,c,*], Fan Zhang [d], Xin Tong [c], Lindong Fan [c], Lu Dai [c]

[a] Changchun Institute of Optics, Fine Mechanics and Physics, Chinese Academy of Sciences, Changchun, 130033, China
[b] University of Chinese Academy of Sciences, Beijing, 100049, China
[c] Chang Guang Satellite Technology Co., LTD, Changchun, 130102, China
[d] School of Automation Science and Electrical Engineering, Beihang University, Beijing, 100191, China

ARTICLE INFO

Keywords:
Optical remote sensing satellites
Attitude planning
Fast maneuver control
Control energy constraint
On-orbit validation

ABSTRACT

This paper aims at developing a novel fast attitude maneuver framework for optical remote sensing satellites subject to multiple uncertainties and limited control energy. The proposed framework relies on a two-layer approach, where the first layer provides the agile attitude planning which enforces the satisfaction of the control energy constraint, whereas the second layer, named the special fast maneuver controller, ensures the high-precision attitude tracking by suitably manipulating the agile attitude planning information. In addition, a novel disturbance observer is introduced into the scenario to enhance the robustness of the proposed fast maneuver controller against multiple uncertainties. The uniform ultimate boundedness of the proposed method is analyzed rigorously with the Lyapunov theory. To demonstrate the effectiveness, the proposed method is applied to the fast attitude maneuver of both simulated and real Jilin-1 GaoFen-02 satellite, which shows excellent control performance despite multiple uncertainties and limited control energy.

1. Introduction

With the further development of space remote sensing technology, optical remote sensing satellites with low cost, low power consumption, low weight, and high precision have been widely used in many commercial fields, such as location services, disaster response, and natural resource management [1,2]. The Flock constellation built by Planet Labs is the highest global timeliness medium [2], updating 5 m resolution images at a global scale per day. The Jilin-1 satellite constellation developed by China Chang Guang Satellite Technology Co., Ltd. consists of 54 satellites with the imaging capability of push and sweep, video, nighttime light, and multi-spectrum [3,4]. Compared with communication satellites and navigation satellites, remote sensing satellites need faster maneuverability to cover a wider area such that they can observe more potential targets within a limited observation time interval [5]. Therefore, the ability of the fast maneuver is crucial for remote sensing satellites [6].

To acquire the powerful ability of fast maneuver, various methods using Control Moment Gyroscopes (CMGs) have been developed for spacecraft. For example, to improve the dynamic performance, a constraint function-based Proportional-Integral-Derivative (PID) controller is introduced in Ref. [7], where the adaptive steering logic is employed to address singularity problem of the pyramid CMG configuration. Moreover, for the typical multi-point imaging missions of earth observation satellites, a CMGs torque optimal control method ensuring agile slew maneuver is proposed in Ref. [8], where the attitude maneuver control ability is significantly improved by determining the optimal slew momentum axis of CMGs. In addition, commercial remote sensing satellites WorldView-1/2/3/4 and Pleiades-1A/1B [9,10] mostly use CMGs technology, making sure that the ten times acceleration of the attitude maneuver with accurate targeting and scanning.

However, due to the limited cost, small optical remote sensing satellites generally prefer to use reaction wheels with limited control energy (i.e., the limited momentum, torque, and dynamic characteristics) rather than expensive CMGs. A “Yardstick design” slew trajectory algorithm with torque and momentum constraints is developed for James Webb Space Telescope (JWST) in Ref. [11]. The algorithm enables minimum-time maneuver of JWST while avoiding the excitation of structural modes by planning the angular acceleration to a multi-segment continuous smooth curve. Actually, to avoid the vibration problem, the attitude planning curve of JWST is too smooth to achieve a time-optimal maneuver. Moreover, the lunar observation

* Corresponding author. Changchun Institute of Optics, Fine Mechanics and Physics, Chinese Academy of Sciences, Changchun, 130033, China.
E-mail address: ciomper@163.com (X. Zhong).

https://doi.org/10.1016/j.actaastro.2022.08.050
Received 13 March 2022; Received in revised form 31 July 2022; Accepted 29 August 2022
Available online 5 September 2022

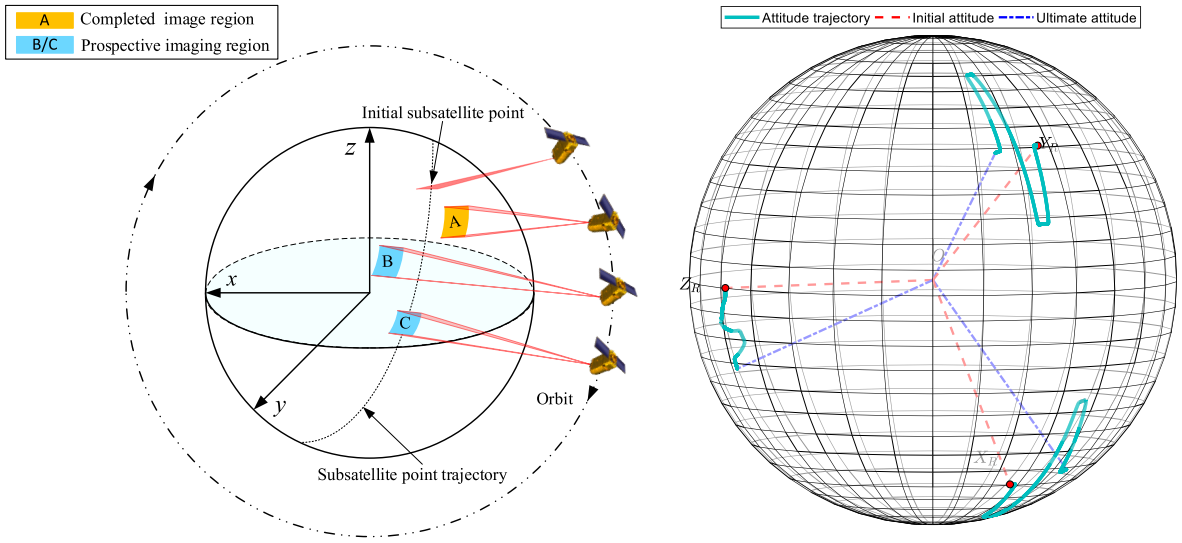

Fig. 1. The same orbit multi-point imaging for optical remote sensing satellites. Left: schematic diagram of multi-point imaging. Right: agile attitude trajectories with three degree-of-freedom on attitude sphere. Red dot: the starting point. (For interpretation of the references to colour in this figure legend, the reader is referred to the Web version of this article.)

satellite Clementine of the United States adopted a Bang-Coast-Bang (BCB) attitude maneuver path scheme combined with a PID controller [12] to accomplish the fast large-angle maneuver. The maneuver angular acceleration path of BCB scheme is divided into three sections (acceleration, uniform speed, and deceleration), which is the optimal solution for attitude maneuver with limited control energy. Nevertheless, it is difficult to meet the control accuracy requirement of optical remote sensing satellites, for there is a slight overshoot in the maneuver process. The similar method is proposed in Ref. [13], where maneuver trajectory is improved by a near time-optimal scheme with Bang-Bang logic. Additionally, an inverse dynamics in the virtual domain attitude planning scheme is developed in Refs. [14,15], which has the excellent performance in both minimum energy and minimum maneuver time control. From the short review above [11–13] and relevant discussions [16–18], designing an agile attitude planning curve subject to limited control energy is the key component in subsequent study attempts to overcome.

On the other hand, even though many methods of the fast maneuver have emerged, the results are still inadequate in the presence of multiple uncertainties (i.e., space environment disturbances and inertia uncertainty). It has been well recognized that the multiple uncertainties are one of the main causes to degrade the control performance [19,20], which is particularly important when imaging of optical remote sensing satellites [21,22]. To overcome this problem, the disturbance observer-based control (DOBC) and related methods [17,23,24] have been implemented in various control systems for disturbance suppression, such as aerospace systems [25–27], mechatronics systems [28,29], and chemical and process control systems [30,31]. The above researches have demonstrated that the principle of disturbance estimation compensation (i.e., treating space environment disturbances and inertia uncertainty as a kind of the lumped disturbance) is an efficient way to cope with the multiple uncertainties. Nevertheless, it is well known that the disturbance observer may cause an impact phenomenon in engineering practice, leading to the performance degradation and instability of the control system. Up to now, the fast maneuver methods with robust disturbance observer have not been investigated for optical remote sensing satellites subject to multiple uncertainties and limited control energy.

In this paper, a novel fast attitude maneuver framework (FAMF) for optical remote sensing satellites subject to multiple uncertainties and limited control energy is developed, achieving the same orbit multi-point imaging mission with excellent time resolution and observation coverage. The main challenges stem from the agile attitude planning, enforcing the satisfaction of the control energy constraint in the considered system. Furthermore, it is worth noting that it is difficult to design parameters as a metric of reaction wheels dynamic characteristics in attitude planning, and few results have been reported. Additionally, the above studies are inadequate in terms of the robustness of disturbance observers, which is very important for practical engineering applications. Compared with the existing results, the main contributions of this paper are summarized as follows.

(1) A novel FAMF relying on an integrating two-layer approach seamlessly is developed to guarantee precision and fast control performance of optical remote sensing satellites subject to multiple uncertainties and limited control energy. The uniform ultimate boundedness of the proposed FAMF is analyzed rigorously by the Lyapunov theory.
(2) Compared with previous attitude planning methods in Refs. [11–13,16] for satellites, this paper designs a novel agile attitude planning which enforces the satisfaction of the limited control energy by introducing specified parameters as a metric of correspondent control energy constraints. In addition, from the macro view, the Bang-Coast-Bang-Smooth (BCBS) logic is designed instead of BCB logic to ensure smooth attitude planning.
(3) A special robust disturbance observer-based fast maneuver controller is designed by suitably manipulating the agile attitude planning information. Moreover, unlike conventional disturbance observers in Refs. [23,24,27], the novel robust disturbance observer is included in the scenario by sigma-modification, which requires no prior information on the system disturbance upper bounds. In essence, the sigma-modification has significant benefits in reducing the peaking phenomenon and adding damping to ensure uniform ultimate boundedness.

The structure of this paper is organized as follows. In section 2, some preliminary knowledge of the same orbit multi-point imaging mission is introduced, which is followed by the attitude dynamics of satellites. Section 3 provides the problem description and several imperative definitions. The proposed FAMF for attitude control and the corresponding analysis are given in Section 4. Simulation studies and real experiments are then shown in Section 5 to show the effectiveness of the proposed control method. Finally, the conclusions are presented in section 6.

2. Preliminaries

In this section, we first illustrate the application significance of the proposed fast maneuver method for the same orbit multi-point imaging. Then, the quaternion-based attitude dynamics with multiple uncertainties of optical remote sensing satellites is presented for the controller design and convergence analysis, which are developed in the subsequent sections.

2.1. The same orbit multi-point imaging

In order to improve the time resolution and observation coverage of optical remote sensing satellite constellation, the same-orbit multi-point imaging mission is developed from the perspective of applications. This imaging mission relies on the fast maneuver method to achieve continuous push-scanning imaging of different imaging targets. The schematic diagram is shown in Fig. 1, where has three prospective imaging targets might be addressed in the future. When the imaging of target A is completed, the satellite must reorientate to target B rapidly within the specified time. Otherwise, target B will be missed, and the imaging task will fail.

In general, the maneuverability of satellites is affected by two factors. The first factor is the control energy, which is irrevocable after satellite manufactured. The second factor is the fast maneuver control method, which is the main research objective of this work.

2.2. Attitude dynamics

Optical remote sensing satellites are usually designed by satellite-payload integration technology. Therefore, the unit quaternion for rigid bodies is suggested to describe the satellite attitude kinematics and dynamics. The dynamics equation can be expressed as follows [5,32]

$$\begin{aligned}\dot{\mathrm{Q}} &= \begin{bmatrix}\dot{q}_0\\ \dot{\mathrm{q}}\end{bmatrix} = \frac{1}{2}\begin{bmatrix}-\mathrm{q}^T\\ \mathrm{S}(\mathrm{q})+q_0\mathrm{I}_3\end{bmatrix}\omega\\ \mathrm{J}\dot{\omega} &= -\mathrm{S}(\omega)(J\omega+\mathrm{h}_w)+\mathrm{u}+\mathrm{d}\end{aligned} \tag{1}$$

where $\mathrm{Q}=(q_0,q_1,q_2,q_3)^T=(q_0,\mathrm{q}^T)^T\in\mathcal{R}\times\mathcal{R}^3$ denotes the quaternion of the body-fixed frame $F_B(O-X_BY_BZ_B)$ with respect to the inertia frame $F_I(O-X_IY_IZ_I)$. In detail, the quaternion satisfies $q_0^2+\mathrm{q}^T\mathrm{q}=1$, and can be represented as $q_0=\cos(\theta/2)$, $\mathrm{q}=\mathrm{e}\sin(\theta/2)$, where the unit vector $\mathrm{e}\in\mathcal{R}^3$ is the Euler axis and $\theta\in\mathcal{R}$ is the Euler angle; $\omega\in\mathcal{R}^3$ denotes the angular velocity of the rigid body with respect to the inertial frame F_I, which is expressed in the body-fixed frame F_B; $\mathrm{J}\in\mathcal{R}^{3\times3}$ denotes the inertia matrix; $\mathrm{u}\in\mathcal{R}^3$ and $\mathrm{h}_w\in\mathcal{R}^3$ denote the control torque and angular momentum of reaction wheels, respectively; $\mathrm{d}\in\mathcal{R}^3$ denotes the space environment disturbances. Besides, for any vector $\mathrm{x}\in\mathcal{R}^3$, $\mathrm{S}(\mathrm{x})\in\mathcal{R}^{3\times3}$ denotes the corresponding antisymmetric matrix as

$$\mathrm{S}(\mathrm{x})=\begin{bmatrix}0 & -x_3 & x_2\\ x_3 & 0 & -x_1\\ -x_2 & x_1 & 0\end{bmatrix} \tag{2}$$

In addition, for the quaternion Q, we can get the corresponding rotation matrix $\mathrm{R}(\mathrm{Q})$ which satisfies $\|\mathrm{R}(\mathrm{Q})\|=1$ is given by

$$\begin{aligned}\mathrm{R}(\mathrm{Q}) &= (q_0^2-\mathrm{q}^T\mathrm{q})\mathrm{I}_3+2\mathrm{q}\mathrm{q}^T-2q_0\mathrm{S}(\mathrm{q})\\ \dot{\mathrm{R}}(\mathrm{Q}) &= -\mathrm{S}(\omega)\mathrm{R}(\mathrm{Q})\end{aligned} \tag{3}$$

Assumption 1. [27]. The space environment disturbances such as gravity-gradient, solar radiation pressure, residual magnetic torque, and aerodynamic drags, are assumed to be bounded and slow-varying enough in practice, namely, the space environment disturbances satisfy $\|\mathrm{d}\|\le\overline{d}$ and $\|\dot{\mathrm{d}}\|=0$, where $\overline{d}$ is an unknown positive constant.

In practice, the inertia matrix of satellites is calibrated by a precise measurement instrument, which has a certain calibration error. Besides, the fuel burning of the propulsion will also change the inertia matrix. Let $\widetilde{\mathrm{J}}\in\mathcal{R}^{3\times3}$ denote the error inertia matrix expressed as

$$\widetilde{\mathrm{J}}=\mathrm{J}_m-\mathrm{J} \tag{4}$$

where $\mathrm{J}_m\in\mathcal{R}^{3\times3}$ denotes the nominal measurement value of the inertia matrix.

Assumption 2. The inertia matrix J_m is bounded and positive definite constant, there exists a positive constant $\overline{J}_m$ such that $\|\mathrm{J}_m\|\le\overline{J}_m$ and $\|\dot{\mathrm{J}}_m\|=0$. Error inertia matrix $\widetilde{\mathrm{J}}$ is unknown but bounded constant, there exist unknown positive constants $\overline{J}_e$ such that $\|\widetilde{\mathrm{J}}\|\le\overline{J}_e$ and $\|\dot{\widetilde{\mathrm{J}}}\|=0$.

Remark 1. Generally, the measurement error of the inertia matrix can be less than 10%, which doesn't change the characteristic of the inertia matrix J_m, hence J_m guarantees the positive definiteness is the same as J, and $\widetilde{\mathrm{J}}$ is bounded. Additionally, the error inertia matrix $\widetilde{\mathrm{J}}$ changing caused by the fuel burning is slow-varying enough in practice, hence $\|\dot{\widetilde{\mathrm{J}}}\|=0$ is reasonable.

3. Problem formulation

Considering the same orbit multi-point imaging illustrated in Section 2.1 and multiple uncertainties items illustrated in Section 2.2, the control problems in this paper can be described as follows. Substituting (4) into (1), the mathematical model can be rewritten in a general form as

$$\begin{aligned}\dot{\mathrm{Q}} &= \begin{bmatrix}\dot{q}_0\\ \dot{\mathrm{q}}\end{bmatrix} = \frac{1}{2}\begin{bmatrix}-\mathrm{q}^T\\ \mathrm{S}(\mathrm{q})+q_0\mathrm{I}_3\end{bmatrix}\omega\\ \mathrm{J}_m\dot{\omega} &= -\mathrm{S}(\omega)(\mathrm{J}_m\omega+\mathrm{h}_w)+\mathrm{u}+\mathrm{d}_l\end{aligned} \tag{5}$$

where $\mathrm{d}_l\in\mathcal{R}^3$ denotes the lumped disturbance, which given as

$$\mathrm{d}_l=\mathrm{d}+\widetilde{\mathrm{J}}\dot{\omega}+\mathrm{S}(\omega)\widetilde{\mathrm{J}}\omega \tag{6}$$

According to **Assumptions 1** and **2,** we can get the derivative of d_l as

$$\dot{\mathrm{d}}_l=\widetilde{\mathrm{J}}\ddot{\omega}+\mathrm{S}(\dot{\omega})\widetilde{\mathrm{J}}\omega+\mathrm{S}(\omega)\widetilde{\mathrm{J}}\dot{\omega} \tag{7}$$

On the other hand, the control energy constraints should be considered in the attitude planning process, where the angular acceleration constraint is given as

$$|\dot{\omega}_i|\le\overline{\dot{\omega}}_i=\frac{\overline{u}_i}{J_i}-\delta_1,\quad i=x,y,z \tag{8}$$

where x,y,z denote the euler axis of satellites; $\dot{\omega}_i\in\mathcal{R}$, $\overline{\dot{\omega}}_i\in\mathcal{R}$, $i=x,y,z$ denote angular acceleration and its theoretical maximum, respectively; $\overline{u}_i\in\mathcal{R}$, $i=x,y,z$ denotes the maximum control torque of reaction wheels; $J_i\in\mathcal{R}$, $i=x,y,z$ denotes the principal axis inertia of satellites; $\delta_1\in\mathcal{R}$ denotes the negative effect of coupling dynamics and the lumped disturbance on maximum angular acceleration. The angular velocity constraint is given as

$$|\omega_i|\le\overline{\omega}_i=\frac{\overline{h}_i}{J_i}-\delta_2,\quad i=x,y,z \tag{9}$$

where $\omega_i\in\mathcal{R}$, $\overline{\omega}_i\in\mathcal{R}$, $i=x,y,z$ denote the angular velocity and its theoretical maximum, respectively; $\overline{h}_i\in\mathcal{R}$, $i=x,y,z$ denotes the maximum control momentum of reaction wheels; $\delta_2\in\mathcal{R}$ denotes the negative effect of coupling dynamics on the maximum angular velocity.

Assumption 3. The lumped disturbance d_l and its derivative $\dot{\mathrm{d}}_l$ are bounded, there exist unknown positive constants $\overline{d}_l$, $\overline{\dot{d}}_l$ such that $\|\mathrm{d}_l\|\le\overline{d}_l$, $\|\dot{\mathrm{d}}_l\|\le\overline{\dot{d}}_l$.

Remark 2. Considering the discussions above, the lumped disturbance in (5) comes from the space environment disturbances and inertia

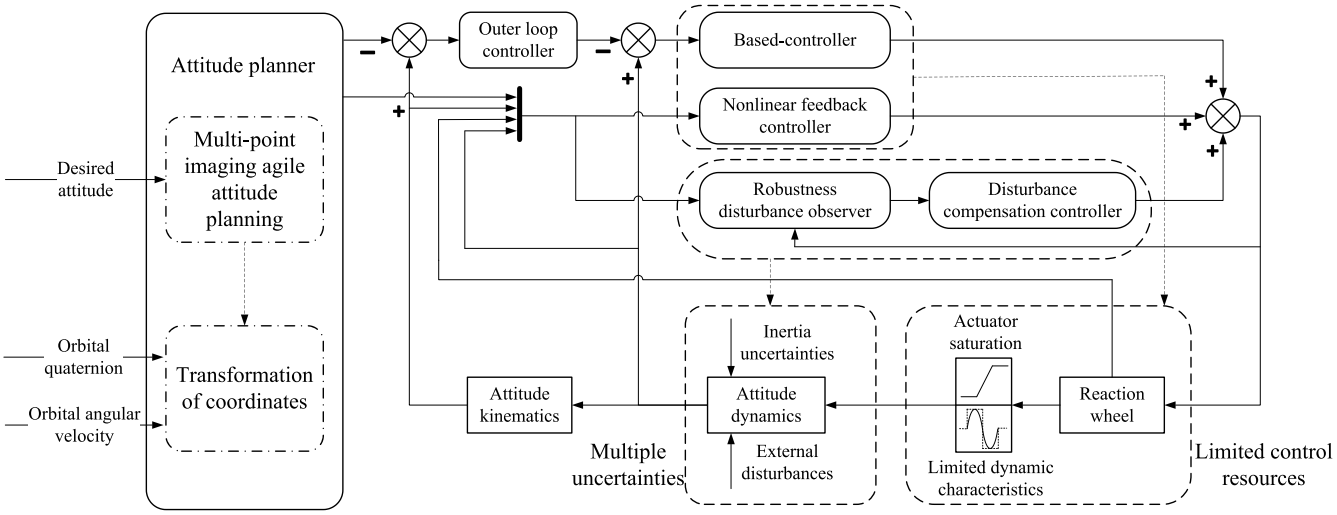

Fig. 2. Fast maneuver controller structure diagram.

uncertainty. Equation (8) and (9), **Assumption 1**, and **Assumption 2** indicate that $\mathrm{d}, \widetilde{\mathrm{J}}, \dot{\omega}, \omega$ are all bounded, which means that the lumped disturbance d_l is bounded. Besides, $\ddot{\omega}$ is bounded for the dynamic characteristics of the reaction wheel is bounded in practice, hence the derivative of the lumped disturbance $\dot{\mathrm{d}}_l$ in (7) is bounded. Therefore, **Assumption 3** is reasonable.

Assumption 4. We assume δ_1 in (8) and δ_2 in (9) are small positive constants.

Remark 3. In practical engineering, the influence of coupling dynamics for optical remote sensing satellites is very small. In addition, the lumped disturbance is generally far less than the control torque of reaction wheels, which can be confirmed by the analysis of on-orbit data. Hence, the maximum angular acceleration and velocity in (8) and (9) are mainly affected by three factors: the principal axis inertia of satellites, the maximum angular momentum and torque of reaction wheels. So, **Assumption 4** is reasonable. Of course, We will consider the influence of δ_1 and δ_2 in the subsequent work.

The first aim of this paper is to ensure the fast attitude maneuver in the presence of the limited control energy described in equations (8) and (9). The second is to restrain the effect of multiple uncertainties, i.e., the lumped disturbance described in equation (5) to ensure precision control performance.

4. Attitude planner and controller design

In this section, the novel FAMF decomposing into attitude planning and tracking control is developed for the satellite system in (5). As shown in Fig. 2, the attitude planner enforces the satisfaction of the energy constraint, and then generates attitude planning information according to the desired attitude, orbit quaternion, and orbit angular velocity. The special fast maneuver controller composed of outer loop controller, based-controller, nonlinear feedback controller, robust disturbance observer, and compensation controller is designed by suitably manipulating the attitude planning information. Thus, the attitude planning and tracking control are integrated seamlessly to ensure precision and fast attitude maneuver.

Remark 4. The orbital quaternion and orbital angular velocity are calculated by the satellite's six orbital elements, which are easy to get from GPS equipped with satellites.

4.1. Attitude planner design and error dynamics

The same orbit multi-point imaging mission described in section 2.1 is a continuous push-scanning imaging process for different imaging targets by the fast lateral swing of satellites. In order to realize the fast maneuver of lateral swing angle, the following agile attitude planning, which enforces the satisfaction of the control energy constraint, is developed by Bang-Coast-Bang-Smooth logic. This work is presented as follows:

$$\begin{cases} \theta_x^d(k+1) = \theta_x^d(k) + T\omega_x^d(k) \\ \omega_x^d(k+1) = \omega_x^d(k) + Ta_x^d(k) \end{cases} \tag{10}$$

where $k \in \mathbb{R}$ denotes the planning index; $T \in \mathbb{R}$ denotes control step; $\theta_x^d \in \mathbb{R}$ denotes planning desired lateral swing angle; $\omega_x^d \in \mathbb{R}$ denotes planning desired lateral swing angular velocity; $a_x^d \in \mathbb{R}$ denotes planning desired lateral swing angular acceleration is designed as

$$a_x^d = \begin{cases} -r_x^l sign(a) & |a| > r_x^l h, |\omega_x^d| < \omega_x^l, \text{or} \\ & |a| > r_x^l h, |\omega_x^d| \geq \omega_x^l, -\omega_x^d sign(a) \leq 0 \\ -a/h & |a| \leq r_x^l h, |\omega_x^d| < \omega_x^l, \text{or} \\ & |a| \leq r_x^l h, |\omega_x^d| \geq \omega_x^l, -\omega_x^d a \leq 0 \\ 0 & \text{other} \end{cases} \tag{11}$$

where $r_x^l \in \mathbb{R}$ denotes the set maximum maneuver angular acceleration; $\omega_x^l \in \mathbb{R}$ denotes the set maximum maneuver angular velocity; $h \in \mathbb{R}$ denotes the smoothing parameter of attitude planner; a is a intermediate variable as

$$a = \begin{cases} \omega_x^d + 0.5\left(\sqrt{\left(r_x^l h\right)^2 + 8r_x^l|y|} - r_x^l h\right)\text{sign}(y), |y| > r_x^l h^2 \\ \omega_x^d + y/h, |y| \leq r_x^l h^2 \end{cases} \tag{12}$$
$$y = \left(\theta_x^d - \theta_v\right) + h\omega_x^d$$

where $\theta_v \in \mathbb{R}$ denotes the desired lateral swing angle.

According to the planning desired lateral swing angle θ_x^d, angular velocity ω_x^d, and angular acceleration a_x^d, the desired attitude quaternion $\mathrm{Q}_d^{bo} \in \mathbb{R} \times \mathbb{R}^3$, angular velocity $\omega_d^{bo} \in \mathbb{R}^3$ and angular acceleration $\mathrm{a}_d^{bo} \in \mathbb{R}^3$ of the body-fixed frame $F_B(O - X_B Y_B Z_B)$ with respect to the orbital frame $F_o(O - X_o Y_o Z_o)$ can be calculated as

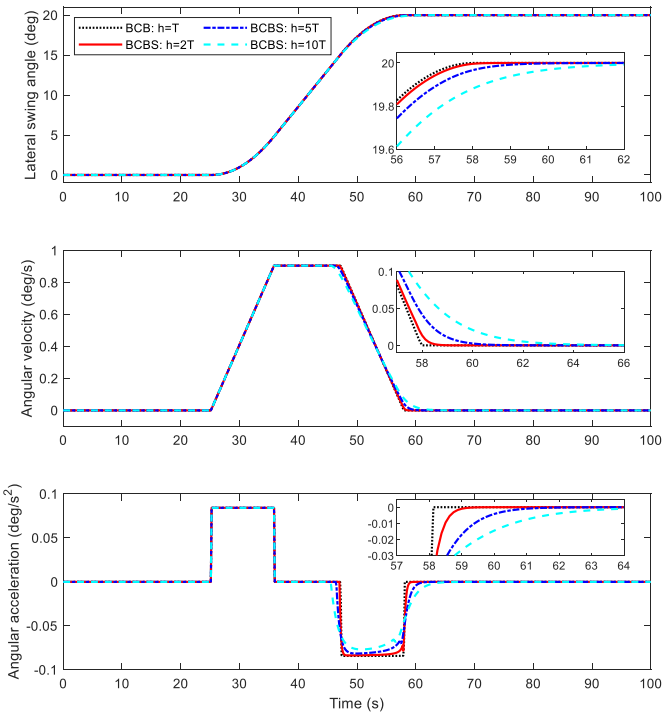

Fig. 3. Planning lateral swing angle, angular velocity and angular acceleration of BCB and BCBS.

$$\begin{aligned} \mathrm{Q}_d^{bo} &= \left[\cos\frac{\theta_x^d}{2} \quad \sin\frac{\theta_x^d}{2} \quad 0 \quad 0\right]^T \\ \omega_d^{bo} &= \left[\omega_x^d \quad 0 \quad 0\right]^T \\ \mathrm{a}_d^{bo} &= \left[a_x^d \quad 0 \quad 0\right]^T \end{aligned} \tag{13}$$

The satellite attitude control system is designed in the inertial frame. According to the desired attitude quaternion Q_d^{bo}, angular velocity ω_d^{bo} and angular acceleration a_d^{bo} in (13), the desired attitude quaternion $\mathrm{Q}_d \in \mathbb{R}\times\mathbb{R}^3$, angular velocity $\omega_d \in \mathbb{R}^3$ and angular acceleration $\mathrm{a}_d \in \mathbb{R}^3$ of the body-fixed frame F_B with respect to the inertia frame F_I can be calculated as

$$\begin{aligned} \mathrm{Q}_d &= \mathrm{Q}^{oI} \otimes \mathrm{Q}_d^{bo} \\ \omega_d &= \omega_d^{bo} + \mathrm{R}\left(\mathrm{Q}_d^{bo}\right)\omega_o \\ \mathrm{a}_d &= \mathrm{a}_d^{bo} = \dot{\omega}_d \end{aligned} \tag{14}$$

where $\mathrm{Q}^{oI} \in \mathbb{R}\times\mathbb{R}^3$ and $\omega_o \in \mathbb{R}^3$ denote the attitude and angular velocity of the orbital frame $F_o(O-X_oY_oZ_o)$ with respect to the inertia frame F_I, respectively.

Let $\mathrm{Q}_e \in \mathbb{R}\times\mathbb{R}^3$ and $\omega_e \in \mathbb{R}^3$ be the quaternion error and the angular velocity error as

$$\begin{aligned} \mathrm{Q}_e &= \mathrm{Q}_d^{-1} \otimes \mathrm{Q} \\ \omega_e &= \omega - \mathrm{R}(\mathrm{Q}_e)\omega_d \end{aligned} \tag{15}$$

where $\mathrm{Q}_d^{-1} \in \mathbb{R}\times\mathbb{R}^3$ denotes the inverse of Q_d; $\otimes$ denotes multiplication operation of quaternion.

The rotation matrix $\mathrm{R}(\mathrm{Q}_e)$ is calculated by (3) as

$$\begin{aligned} \mathrm{R}(\mathrm{Q}_e) &= \left(q_{e0}^2 - \mathrm{q}_e^T\mathrm{q}_e\right)\mathrm{I}_3 + 2\mathrm{q}_e\mathrm{q}_e^T - 2q_{e0}\mathrm{S}(\mathrm{q}_e) \\ \dot{\mathrm{R}}(\mathrm{Q}_e) &= -\mathrm{S}(\omega_e)\mathrm{R}(\mathrm{Q}_e) \end{aligned} \tag{16}$$

Based on the attitude dynamics in (1), the quaternion error and the angular velocity error in (15), and the error rotation matrix in (16), the error dynamics is given as

$$\begin{aligned} \dot{\mathrm{Q}}_e &= \begin{bmatrix} \dot{q}_{e0} \\ \dot{\mathrm{q}}_e \end{bmatrix} = \frac{1}{2}\begin{bmatrix} -\mathrm{q}_e^T \\ \mathrm{S}(\mathrm{q}_e) + q_{e0}\mathrm{I}_3 \end{bmatrix}\omega_e \\ \mathrm{J}_m\dot{\omega}_e = & -\mathrm{S}(\omega)(\mathrm{J}_m\omega + \mathrm{h}_w) + \mathrm{J}_m\mathrm{S}(\omega_e)\mathrm{R}(\mathrm{Q}_e)\omega_d \\ & -\mathrm{J}_m\mathrm{R}(\mathrm{Q}_e)\dot{\omega}_d + \mathrm{u} + \mathrm{d}_l \end{aligned} \tag{17}$$

Remark 5. It should be noted that r_x^l and ω_x^l in (11) are the parameters of the attitude planning, and they should meet the constraints in (8) and (9) respectively. To ensure fast attitude maneuver, the previous method using the BCB strategy cannot be realized in the actual physical system for the limited dynamic characteristics of reaction wheels. Hence, the BCBS logic is designed by setting the smoothing parameter h in (11). As shown in Fig. 3, the agile attitude planning is equal to BCB when $\mathrm{h} = \mathrm{T}$, and with the larger the parameter h is, the smoother the attitude planning is. Of course, the parameter h cannot be too large, because the parameter design should consider both stability and rapidity. Thus, the control energy constraint and maneuverability are comprehensively designed in the attitude planning process.

4.2. Attitude controller design and convergence analysis

To ensure the attitude control performance of optical remote sensing satellites with multiple uncertainties, the robust disturbance observer-based fast maneuver controller is developed. The attitude tracking controller is divided into outer loop controller and inner loop controller ensuring the objective of high-precision attitude tracking. According to the error dynamics in (17), the outer loop controller is designed as

$$\omega_e^v = -K_q\mathrm{q}_e \tag{18}$$

where $K_q \in \mathbb{R}$ is outer loop attitude controller gain; $\omega_e^v \in \mathbb{R}^3$ denotes virtual control signal.

From (14), (17) and (18), the inner loop controller is designed as

$$\mathrm{u} = \mathrm{u}_b + \mathrm{u}_f + \mathrm{u}_d \tag{19}$$

where $\mathrm{u}_b \in \mathbb{R}^3$ denotes based-controller; $\mathrm{u}_f \in \mathbb{R}^3$ denotes nonlinear feedback controller; $\mathrm{u}_d \in \mathbb{R}^3$ denotes disturbance compensation controller. The specific form of each controller is

$$\begin{aligned} \mathrm{u}_b = & -K_\omega\mathrm{J}_m\tilde{\omega}_e \\ \mathrm{u}_f = & \ \mathrm{S}(\omega)(\mathrm{J}_m\omega + \mathrm{h}_w) - \mathrm{J}_m\mathrm{S}(\omega_e)\mathrm{R}(\mathrm{Q}_e)\omega_d + \mathrm{J}_m\mathrm{R}(\mathrm{Q}_e)\dot{\omega}_d \\ & -\mathrm{J}_m\mathrm{q}_e - \frac{1}{2}K_q\mathrm{J}_m(\mathrm{S}(\mathrm{q}_e) + q_{e0}\mathrm{I}_3)\omega_e \\ \mathrm{u}_d = & -\hat{\mathrm{d}}_l \end{aligned} \tag{20}$$

where $K_\omega \in \mathbb{R}$ is the inner loop attitude controller gain; $\tilde{\omega}_e \in \mathbb{R}^3$ denotes the virtual angular velocity tracking error calculated by $\tilde{\omega}_e = \omega_e - \omega_e^v$; $\hat{\mathrm{d}}_l \in \mathbb{R}^3$ denotes the estimation of the lumped disturbance.

To deal with the bounded lumped disturbance, a robust disturbance observer is developed, which has significant benefits in reducing the peaking phenomenon and adding damping to ensure uniform ultimate boundedness. The disturbance observer is designed as

$$\begin{aligned} \hat{\mathrm{d}}_l = & \ \mathrm{p} + L\mathrm{J}_m\omega_e \\ \dot{\mathrm{p}} = & -L(\mathrm{p} + L\mathrm{J}_m\omega_e) - L(-\mathrm{S}(\omega)(\mathrm{J}_m\omega + \mathrm{h}_w) + \mathrm{J}_m\mathrm{S}(\omega_e)\mathrm{R}(\mathrm{Q}_e)\omega_d) \\ & -L(-\mathrm{J}_m\mathrm{R}(\mathrm{Q}_e)\dot{\omega}_d + \mathrm{u}) - \sigma\hat{\mathrm{d}}_l \end{aligned} \tag{21}$$

where $L \in \mathbb{R}$ is disturbance observer gain; $\sigma \in \mathbb{R}$ is sigma-modification gain; $\mathrm{p} \in \mathbb{R}^3$ denotes auxiliary variable of the disturbance observer. Let estimation error of disturbance observer $\tilde{\mathrm{d}}_l \in \mathbb{R}^3$ as

$$\tilde{\mathrm{d}}_l = \hat{\mathrm{d}}_l - \mathrm{d}_l \tag{22}$$

Theorem 1. *For error dynamics subject to multiple uncertainties in (17), let controller in (18) and (19), and disturbance observer in (21) be applied. Then, it is shown that all system variables are uniformly ultimate bounded, and the robust fast maneuver for attitude control can be achieved.*

Proof. Choose the Lyapunov function V as

$$V = V_1 + V_2 + V_3 \tag{23}$$

where

$$\begin{aligned} V_1 &= \mathrm{q}_e^T \mathrm{q}_e + (1 - q_{e0})^2 \\ V_2 &= \frac{1}{2}\widetilde{\omega}_e^T \widetilde{\omega}_e \\ V_3 &= \frac{1}{2}\widetilde{\mathrm{d}}_l^T \widetilde{\mathrm{d}}_l \end{aligned} \tag{24}$$

According to (17), differentiating V_1 in (24) results in

$$\dot{V}_1 = 2\mathrm{q}_e^T \dot{\mathrm{q}}_e - 2(1 - q_{e0})\dot{q}_{e0} = \mathrm{q}_e^T(\mathrm{S}(\mathrm{q}_e) + q_{e0}\mathrm{I}_3)\omega_e + (1 - q_{e0})\mathrm{q}_e^T\omega_e \tag{25}$$

From $\widetilde{\omega}_e = \omega_e - \omega_e^v$ and the outer loop controller in (18), we can obtain

$$\omega_e = \widetilde{\omega}_e - K_q \mathrm{q}_e \tag{26}$$

Substituting (26) into (25) leads to

$$\dot{V}_1 = -K_q \mathrm{q}_e^T \mathrm{q}_e + \mathrm{q}_e^T \widetilde{\omega}_e \tag{27}$$

According to (17), (20) and (26), differentiating V_2 in (24) results in

$$\dot{V}_2 = \widetilde{\omega}_e^T \dot{\widetilde{\omega}}_e = -K_\omega \widetilde{\omega}_e^T \widetilde{\omega}_e - \widetilde{\omega}_e^T \mathrm{q}_e - \widetilde{\omega}_e^T \mathrm{J}_m^{-1} \widetilde{\mathrm{d}}_l \tag{28}$$

According to (21), differentiating V_3 in (24) results in

$$\dot{V}_3 = -L\widetilde{\mathrm{d}}_l^T \widetilde{\mathrm{d}}_l - \widetilde{\mathrm{d}}_l^T \dot{\mathrm{d}}_l - \sigma \widetilde{\mathrm{d}}_l^T \widehat{\mathrm{d}}_l \tag{29}$$

Taking sum of (24) and (27)~(29), we have

$$\dot{V} = -K_q \mathrm{q}_e^T \mathrm{q}_e - K_\omega \widetilde{\omega}_e^T \widetilde{\omega}_e - \widetilde{\omega}_e^T \mathrm{J}_m^{-1} \widetilde{\mathrm{d}}_l - L\widetilde{\mathrm{d}}_l^T \widetilde{\mathrm{d}}_l - \widetilde{\mathrm{d}}_l^T \dot{\mathrm{d}}_l - \sigma \widetilde{\mathrm{d}}_l^T \widehat{\mathrm{d}}_l \tag{30}$$

According to Young's inequality and (30), we have

$$\begin{aligned} \dot{V} \le & -K_q \|\mathrm{q}_e\|^2 - K_\omega \left\|\widetilde{\omega}_e\right\|^2 - L\left\|\widetilde{\mathrm{d}}_l\right\|^2 + \frac{1}{2}\|\mathrm{J}_m^{-1}\|\left\|\widetilde{\omega}_e\right\|^2 + \frac{1}{2}\|\mathrm{J}_m^{-1}\|\left\|\widetilde{\mathrm{d}}_l\right\|^2 \\ & + \frac{1}{8}\left\|\widetilde{\mathrm{d}}_l\right\|^2 + 2\|\dot{\mathrm{d}}_l\|^2 - \frac{1}{2}\sigma\left\|\widetilde{\mathrm{d}}_l\right\|^2 + \frac{1}{2}\sigma\|\mathrm{d}_l\|^2 \end{aligned} \tag{31}$$

According to **Assumption 3** *and (31), we further obtain*

$$\dot{V} \le -K_q \|\mathrm{q}_e\|^2 - \left(K_\omega - \frac{1}{2}\|\mathrm{J}_m^{-1}\|\right)\|\widetilde{\omega}_e\|^2 - \left(L - \frac{1}{2}\|\mathrm{J}_m^{-1}\| - \frac{1}{8} + \frac{1}{2}\sigma\right)\|\widetilde{\mathrm{d}}_l\|^2 - K_q(1 - q_{e0})^2 + c_V \tag{32}$$

where

$$c_V = K_q(1 - q_{e0})^2 + \frac{1}{2}\sigma\overline{d}_l^2 + 2\overline{\dot{d}}_l^2 \tag{33}$$

Then we have

$$\dot{V} \le -\mu_V V + \overline{c}_V \tag{34}$$

where

$$\begin{aligned} \mu_V &= \min\left\{K_q, 2\left(K_\omega - \frac{1}{2}\|\mathrm{J}_m^{-1}\|\right), 2\left(L - \frac{1}{2}\|\mathrm{J}_m^{-1}\| - \frac{1}{8} + \frac{1}{2}\sigma\right)\right\} \\ \overline{c}_V &= \sup_{t\ge 0}|c_V| \end{aligned} \tag{35}$$

It is clear that $0 \le V(t) \le \max\left\{\frac{\overline{c}_V}{2\mu_V}, V(0)\right\}$ holds for all $t \ge 0$. Therefore, the boundedness of all the signals can be guaranteed. The proof has been completed. □

Table 1
The satellite parameters.

Parameters	Value
Orbital altitude (Km)	535
Orbital type	Sun-synchronous orbit
Inertia matrix J_m (kg m^2)	$\begin{bmatrix} 54.6 & 0.69 & -0.17 \\ 0.69 & 49.2 & 0.02 \\ -0.17 & 0.02 & 28.7 \end{bmatrix}$
Reaction wheel torque (Nm)	0.1
Reaction wheel momentum (Nm s)	1.2

Remark 6. *The based-controller $\mathrm{u}_b = -K_\omega \mathrm{J}_m \widetilde{\omega}_e$ in (20) can be simplified to $\mathrm{u}_b = -K_q K_\omega \mathrm{J}_m \mathrm{q}_e - K_\omega \mathrm{J}_m \omega_e$, which is a PD controller. Hence to ensure the proposed controller can be applied in practical engineering, the outer loop attitude controller gain K_q and inner loop attitude controller gain K_ω are designed to not only guarantee $\mu_V > 0$ in (35), but follow the frequency response design method of classical control theory in [33].*

Remark 7. *Different from conventional disturbance observers in [23,24,27], the robust disturbance observer in (21) is included in the scenario by sigma-modification, a technique widely used in adaptive control [34,35] to add damping, which ensures uniform ultimate boundedness of the proposed FAMF. Besides, the sigma-modification can reduce the peaking phenomenon.*

5. Simulations and real experiments

In this section, the maneuver efficiency and robustness of the proposed method are demonstrated by numerical simulations and real experiments of the Jilin-1 GaoFen-02 satellite, a high-resolution optical remote sensing satellite. In particular, the high-fidelity dynamics model is used to ensure the validity and feasibility of numerical simulations, including: the star sensor model is established based on the ground star observation experiments; the three-axis fiber optic gyro model is established according to the results of gyro calibration and allan variance analysis; the reaction wheel model is established as second-order elements by model identification.

To be more persuasive, the error quaternion-based PD controller [14] and the robust adaptive controller [19,34] are applied to the simulations. The error quaternion-based PD controller is among the most used controller of satellites, for its simplicity and applicability. The specific form of the PD controller is

$$\mathrm{u} = -\mathrm{J}_m\left(K_p \mathrm{q}_e + K_d \omega_e\right) \tag{36}$$

where $K_p \in \mathbb{R}$ denotes the proportional coefficient; $K_d \in \mathbb{R}$ denotes the derivative coefficient. In particular, we make $|q_{ei}| < \overline{q}, i = 1, 2, 3$ to constrain the angular velocity of the PD controller.

The robust model reference adaptive controller (RMRAC) has excellent command tracking performance and robustness to model uncertainties and environmental disturbances, so it is widely used in aerospace control systems. The RMRAC in this paper is designed as

$$\mathrm{u} = (\mathrm{I}_3 + \widehat{\mathrm{G}})(-K_1 K_2 \mathrm{J}_m \mathrm{q}_e - K_2 \mathrm{J}_m \omega_e - \widehat{\mathrm{d}}_l - \mathrm{J}_m \mathrm{S}(\omega_e)\mathrm{R}(\mathrm{Q}_e)\omega_d + \mathrm{J}_m \mathrm{R}(\mathrm{Q}_e)\dot{\omega}_d) \tag{37}$$

Table 2
The controller parameters.

	Parameter	Value
FAMF	ω_x^l	0.0157
	r_x^l	0.00147
	h	10T
	K_q	0.6
	K_ω	1.5
	L	0.45
	σ	0.05
PD	K_p	0.5
	K_d	1.5
	$\overline{q}$	0.0471
RMRAC	K_1	0.6
	K_2	1.5
	Γ_1, Γ_2	0.5
	σ_1, σ_2	0.05
	p_1, p_2	0.35

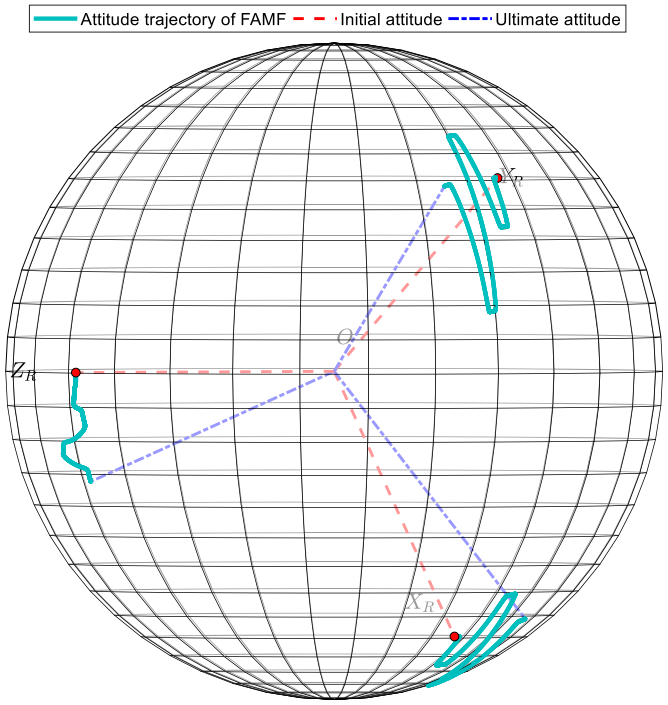

Fig. 4. The attitude trajectories with three degrees-of-freedom on attitude sphere. Red dot: the starting point. (For interpretation of the references to colour in this figure legend, the reader is referred to the Web version of this article.)

with the adaptive laws as

$$\dot{\hat{\mathrm{d}}}_l = \Gamma_1(\omega_e + K_1 \mathrm{q}_e) - \sigma_1 \hat{\mathrm{d}}_l$$
$$\dot{\hat{\mathrm{G}}} = -\Gamma_2 \mathrm{u}_b(\omega_e + K_1 \mathrm{q}_e)^T - \sigma_2 \hat{\mathrm{G}} \tag{38}$$

where $K_1, K_2 \in \mathbb{R}$ denote the control gain; $\Gamma_1, \Gamma_2, \sigma_1, \sigma_2 \in \mathbb{R}$ denote the parameters of adaptive laws. The reference model of RMRAC is a second order element with poles p_1, p_2.

5.1. Simulation parameters

5.1.1. The satellite parameters

The orbital parameters, inertia parameters and reaction wheel parameters of the satellite are shown in Table 1.

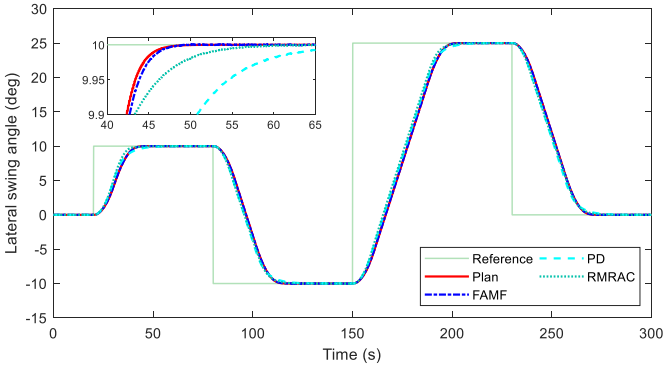

Fig. 5. Lateral swing angle.

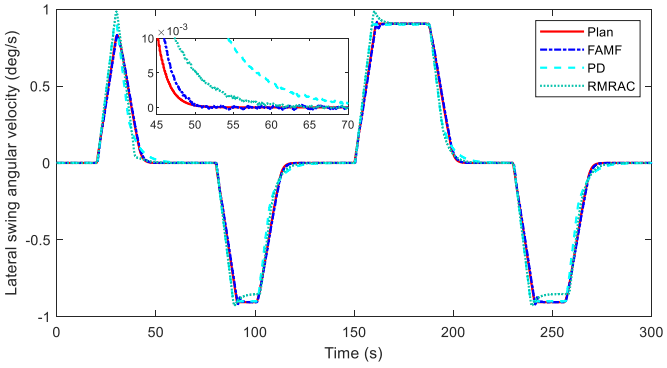

Fig. 6. Lateral swing angular velocity.

5.1.2. The controller parameters

According to the studies described above, the controller parameter design is shown in Table 2. For the attitude planner of FAMF, we design $r_x^l = 0.00147 \leq 0.8\overline{u}_x/J_x$, and $\omega_x^l = 0.0157 \leq 0.75\overline{h}_x/J_x$ for two reasons. The one is to ensure sufficient control torque to cope with multiple uncertainties and coupled dynamics. The other is because it is impossible that the angular momentum of the reaction wheel is zero when the attitude maneuver begins. In general, reaction wheels work in an angular momentum interval when the attitude of satellites is stable, and the rest angular momentum can be used for attitude maneuver. For the based-controller, its amplitude margin $G_m = 20.3\mathrm{dB} > 6\mathrm{dB}$, phase margin $P_m = 70.1\mathrm{deg} \geq 65\mathrm{deg}$ ensure reasonable robustness and rapidity. In addition, the multiple uncertainties change slowly according to the flight data from on-orbit satellites. Therefore, relatively small observer gains are designed considering the suppression of sensor noise.

For PD and RMRAC, their parameters are designed to exert their control ability as much as possible, and ensure the stability of attitude maneuver. Moreover, to achieve the fair comparison, the output torques of all controllers are limited by saturation according to the maximum torque of reaction wheels.

5.2. Simulation results

In order to demonstrate excellent control performance despite multiple uncertainties and limited control energy of the proposed method, the PD and RMRAC method are compared with the proposed FAMF in terms of the maneuver efficiency and robustness. This section conducts simulation analysis on the following three cases.

5.2.1. Case I the maneuver efficiency assessment

Lateral swing to 10°, -10°, 25°, 0° at time = 20 s, 80 s, 150 s 230 s, respectively. In addition, any uncertainty is not considered, namely $\mathrm{J}_m = \mathrm{J}$, $\mathrm{d} = (0,0,0)^T\mathrm{Nm}$.

Table 3
The maneuver efficiency assessment.

Maneuver index and Angle	MEAC.1 (s)			MEAC.2 (s)		
	FAMF	RMRAC	PD	FAMF	RMRAC	PD
No.1 (10°)	27.0 (100%)	30.1 (112%)	37.8 (140%)	29.5 (100%)	37.0 (125%)	47.1 (160%)
No.2 (20°)	38.0 (100%)	43.5 (115%)	49.5 (130%)	40.2 (100%)	49.5 (123%)	58.3 (145%)
No.3 (35°)	54.5 (100%)	58.8 (108%)	65.9 (121%)	56.5 (100%)	64.5 (114%)	75.6 (134%)
No.4 (25°)	43.6 (100%)	49.3 (113%)	54.5 (125%)	45.6 (100%)	54.9 (120%)	63.8 (140%)

As mentioned above, the multi-point imaging mission acquires a series of images for the target area when the attitude maneuver completing. The earlier the maneuver is completed, the wider range of imaging is possible. If the maneuver is too slow, the imaging target may be missed. With the simulation conditions mentioned in **Case I**, the maneuver efficiency of three control methods will be assessed with the following two maneuver efficiency assessment criteria (MEAC). The one (MEAC.1) is the basic imaging condition with pointing accuracy errors less than 0.05°, and attitude stability errors less than 0.005°/ s. The other (MEAC.2) is the excellent imaging condition with pointing accuracy errors less than 0.01°, and attitude stability errors less than 0.001°/ s.

The attitude trajectories are shown in Figs. 4–6. Fig. 4 shows the attitude trajectories with three degree-of-freedom on the attitude sphere, and Figs. 5 and 6 show the lateral swing angle and angular velocity trajectories of the same orbit multi-point imaging. The proposed FAMF method can achieve accurate and stable tracking control for all the maneuvers. Meanwhile, the angular velocity of FAMF converges to a steady state rapidly at the end of the maneuver. Whereas the angular velocity trajectories of PD and RMRAC are also steady but relatively slow.

According to the attitude trajectories and two MEAC, the attitude maneuver time is counted in Table 3. To quantify the maneuver efficiency, the attitude maneuver time of FAMF is considered as a benchmark for comparison at 100%, and the comparison bar chart is shown in Fig. 7. Obviously, FAMF, RMRAC and PD vary considerably in level of maneuver efficiency. In general, FAMF ensures the highest degree, RMRAC followed and PD worst. The bar chart indicates that FAMF has obvious advantages in the small angle maneuver. With the increase of maneuver angle, the advantage of FAMA decreases by a small amount, for the maneuver time of large angle depends more on the maximum angular velocity. Specifically, according to the left chart in maneuver 10°, FAMF has 12% and 40% advantages over RMRAC and PD, respectively. Whereas in maneuver 35°, FAMF has only 8% and 21% advantages. On the other hand, FAMF by MEAC.2 gives clearly better results

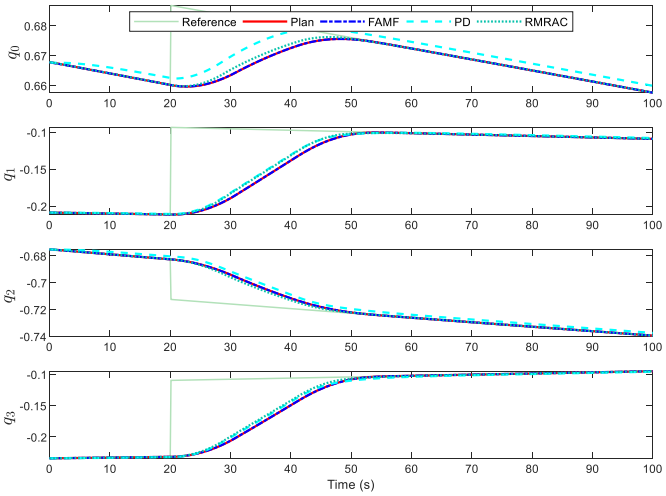

Fig. 8. Attitude quaternion.

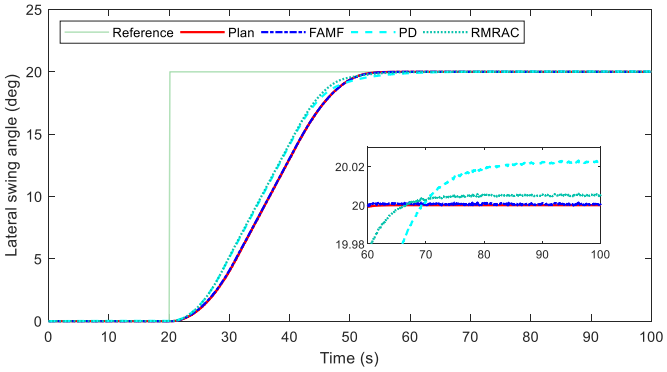

Fig. 9. Lateral swing angle.

by comparing the differences between the left chart and right chart in Fig. 7, namely, FAMF has the advantage in achieving high quality and fast imaging. For example, in maneuver 10°, FAMF by MEAC.1 has 12% and 40% advantages over RMRAC and PD, respectively, when by MEAC.2 has 25% and 60% advantages.

5.2.2. *Case II the robustness assessment of time-invariant uncertainties*

Lateral swing to 20° at time = 20 s and existing constant space environment disturbances without considering inertia uncertainty,

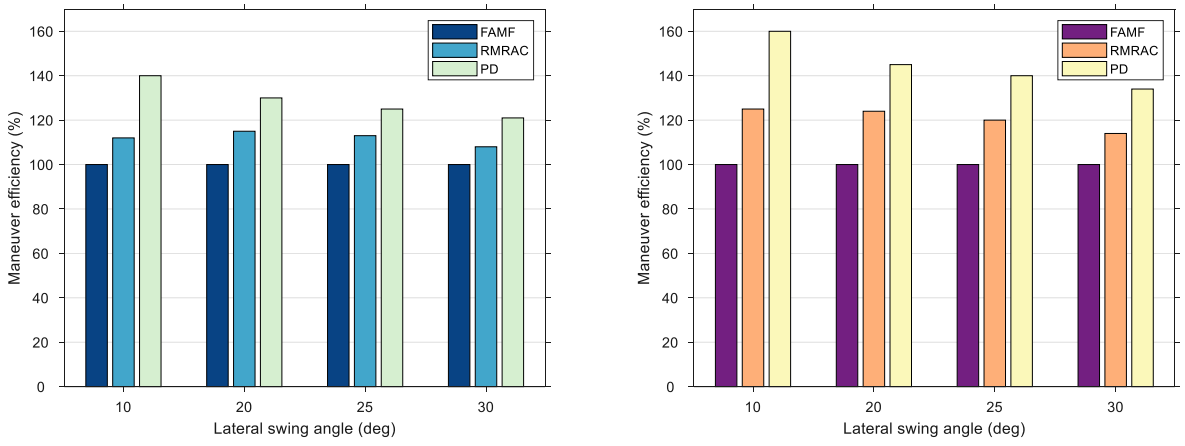

Fig. 7. The bar chart of maneuver efficiency assessment. Left: MEAC.1. Right: MEAC.2.

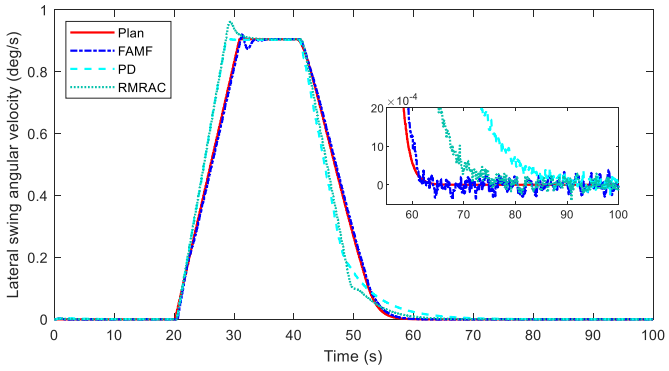

Fig. 10. Lateral swing angular velocity.

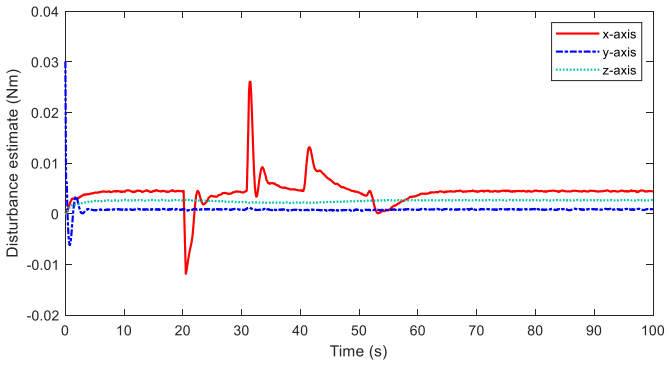

Fig. 11. Disturbance estimate.

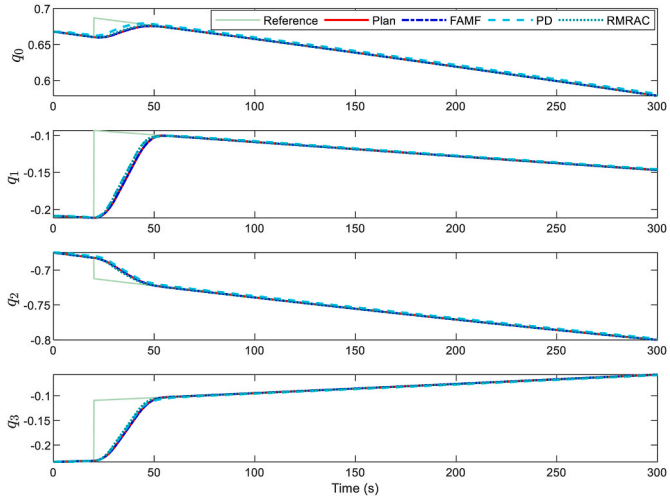

Fig. 12. Attitude quaternion.

namely, $J_m = J$, $d = (0.005, 0.001, 0.003)^T$Nm.

With the parameter settings mentioned in **Case II**, the simulation results are shown in Figs. 8–11. The attitude quaternion is shown in Fig. 8, and lateral swing angle is shown in Fig. 9, where the attitude tracking control trajectories of FAMF are smooth and accurate. In contrast, the PD and RMRAC have 0.021° and 0.005° pointing accuracy errors, respectively. The pointing accuracy errors of RMRAC have little effect on imaging, but PD does not meet excellent imaging condition with pointing accuracy errors less than 0.01°. Lateral swing angular velocity is shown in Fig. 10, where the angular velocity trajectories of three control methods are smooth, showing time invariant uncertainties have no effect on angular velocity control. The disturbance estimate is

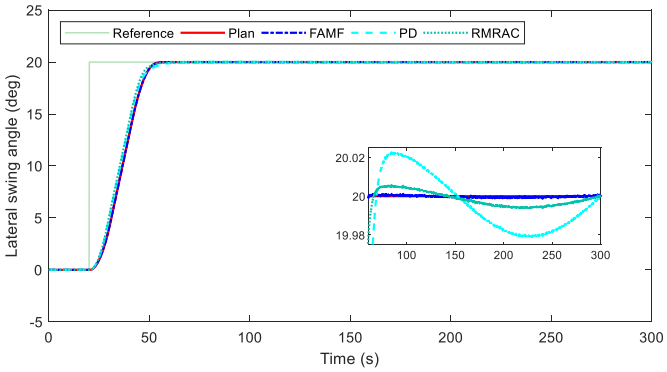

Fig. 13. Lateral swing angle.

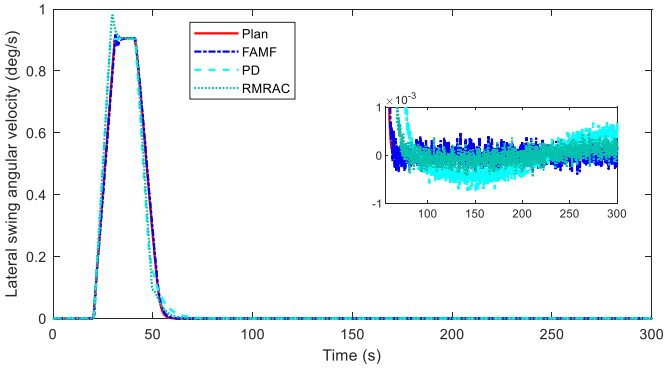

Fig. 14. Lateral swing angular velocity.

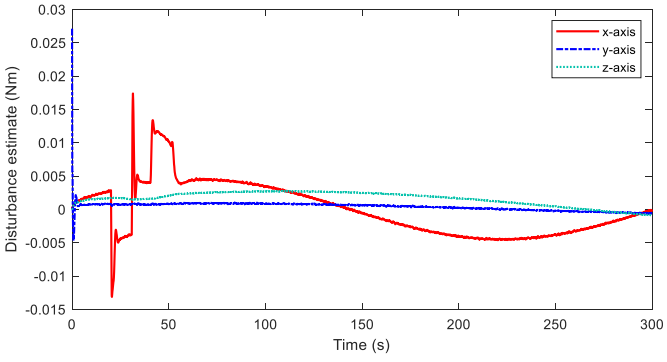

Fig. 15. Disturbance estimate.

shown in Fig. 11, which is the key for FAMF to achieve accurate tracking control.

5.2.3. *Case III the robustness assessment of time-variant uncertainties*

Lateral swing 20° at time = 20 s, inertia uncertainty is −10% and existing slow variable space environment disturbances, namely $J_m = 0.9J$, $d = (d_1, d_2, d_3)^T$Nm, where $d_i = a_i \sin(\varsigma_i t + \varphi_i), i = 1, 2, 3$, $a_1 = 0.005$, $a_2 = 0.001$, $a_2 = 0.003$, $\varsigma_1 = 0.02$, $\varsigma_2 = 0.03$, $\varsigma_3 = 0.01$, $\varphi_1 = 0.3$, $\varphi_2 = 0.9$, $\varphi_3 = 0.5$.

With the parameter settings mentioned in **Case III**, the simulation results are shown in Figs. 12–15-. The attitude quaternion is shown in Fig. 12. Lateral swing angle and angular velocity are shown in Fig. 13 and Fig. 14, respectively. The same as shown in **Case II**, the lateral swing angle and angular velocity trajectories of FAMF are smooth and accurate despite time variant uncertainties. A little worse is RMRAC has 0.005° dynamic errors of pointing accuracy, but its angular velocity trajectories are not affected by time variant uncertainties. The worst is PD, which

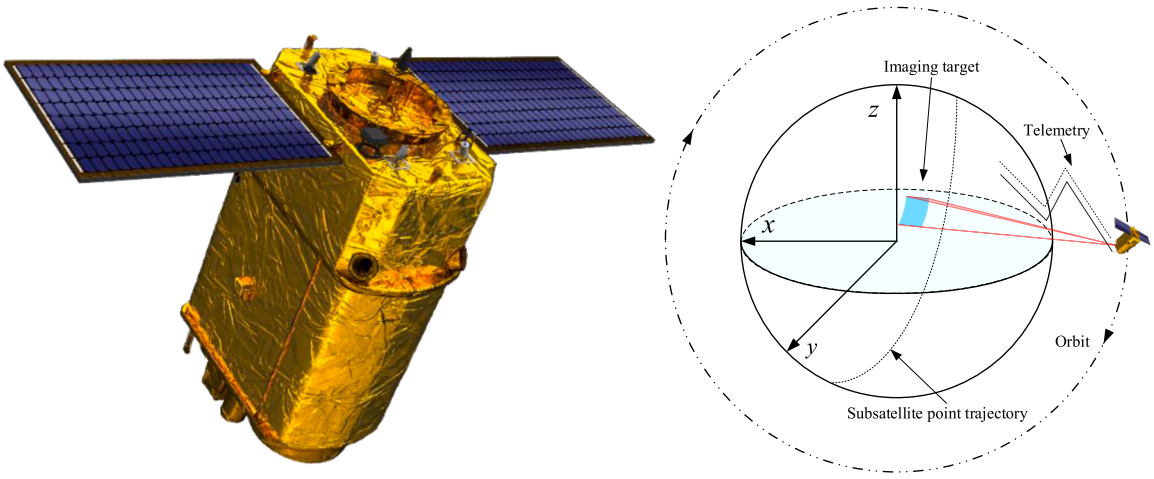

Fig. 16. Jilin-1 GaoFen-02 satellite model and mission schematic diagram.

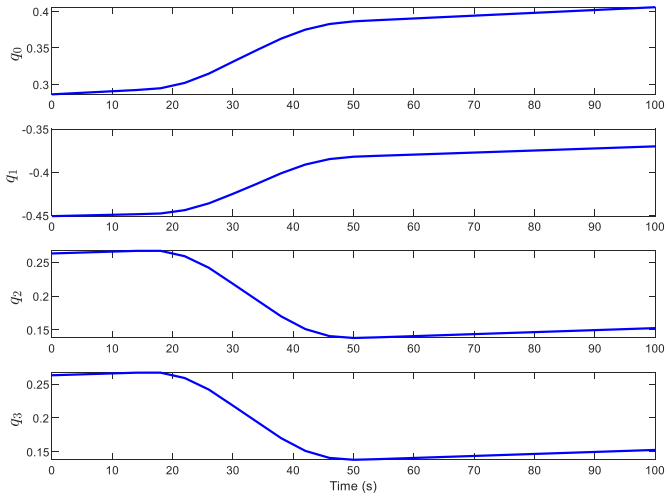

Fig. 17. Attitude quaternion of real experiments.

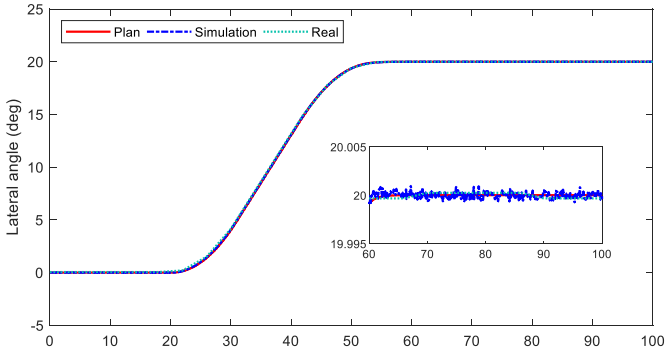

Fig. 18. Lateral swing angle of real experiments and simulations.

has 0.022° dynamic errors of pointing accuracy and 0.0006°/ s dynamic errors of attitude stability, leading to degradation of imaging quality. The disturbance estimate is shown in Fig. 15, where time variant uncertainties are estimated and compensated.

5.3. Real experiments

The proposed method has been applied to the Jilin-1 GaoFen-02 satellite. The satellite model and real experimental schematic diagram

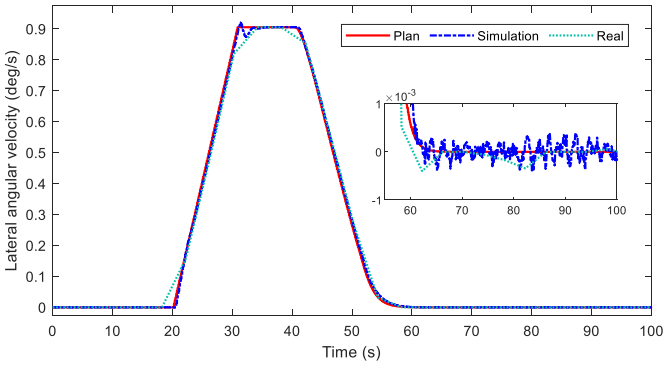

Fig. 19. Lateral swing angular velocity of real experiments and simulations.

are shown in Fig. 16. The telemetry data of satellite attitude maneuver control are received by Changchun Station by the mission within the satellite telemetry circle, where carried out the fast maneuver control experiment of lateral swing 20° at time = 20 s.

The attitude quaternion is shown in Fig. 17. Lateral swing angle and angular velocity are shown in Fig. 18 and 19, respectively. It is evident that the trajectories of simulations and real experiments are consistent, whether control precision or maneuver time. Meanwhile, the pointing accuracy errors and attitude stability errors of real experiments are 0.001° and 0.0005°/s, respectively, which are far better than excellent imaging condition with pointing accuracy errors less than 0.01°, and attitude stability errors less than 0.001°/s. In general, the real experiments prove the excellent performance of the proposed method. On the other hand, owing to the simulations and real experiments are consistent, the simulation results can be the reference in the process of imaging mission planning.

6. Conclusions

In this paper, a novel FAMF has been proposed for attitude control of optical remote sensing satellites subject to multiple uncertainties and limited control energy. Based on the same orbit multi-point imaging mission, the agile attitude planning which enforces the satisfaction of the energy constraint is developed, providing sufficient references for controller design. Then, the special fast maneuver controller, ensures the high-precision attitude tracking by suitably manipulating the agile attitude planning information. Moreover, a novel robust disturbance observer is introduced to enhance the robustness of FAMF against multiple uncertainties, while reducing the peaking phenomenon and

adding damping. Subsequently, the uniform ultimate boundedness of the proposed controller is analyzed rigorously with the Lyapunov theory. Finally, the simulations and real experiments of Jilin-1 Gaofen-02 satellite assess the maneuver efficiency and robustness of three control methods. The analysis of the simulations shows that FAMF has more advantages than other control methods. The real experiments of FAMF indicate that the control results of the simulations and real experiments are consistent, and the pointing accuracy errors and attitude stability errors are far better than the excellent imaging condition. At present, the FAMF has become a mature control mode, improving the time resolution and observation coverage of remote sensing optical satellites.

Declaration of competing interest

The authors declare that they have no known competing financial interests or personal relationships that could have appeared to influence the work reported in this paper.

Acknowledgement

This work was supported in part by the National Key Research and Development Program of China No.2019YFE0127000.

References

[1] D. Selva, D. Krejci, A survey and assessment of the capabilities of Cubesats for Earth observation, Acta Astronaut. 74 (2012) 50–68, https://doi.org/10.1016/j.actaastro.2011.12.014.
[2] J.R. Kopacz, R. Herschitz, J. Roney, Small satellites an overview and assessment, Acta Astronaut. 170 (2020) 93–105, https://doi.org/10.1016/j.actaastro.2020.01.034.
[3] Y. Luo, L. Zhou, S. Wang, Z. Wang, Video satellite imagery super resolution via convolutional neural networks, Geosci. Rem. Sens. Lett. IEEE 14 (2017) 2398–2402, https://doi.org/10.1109/LGRS.2017.2766204.
[4] Q. Zheng, Q. Weng, L. Huang, K. Wang, J. Deng, R. Jiang, Z. Ye, M. Gan, A new source of multi-spectral high spatial resolution night-time light imagery—JL1-3B, Rem. Sens. Environ. 215 (2018) 300–312, https://doi.org/10.1016/j.rse.2018.06.016.
[5] L. Zhao, K. Zhao, Y. Hao, X. Zhang, Y. He, The attitude control algorithm of agile optical satellite oriented to nonparallel-ground-track-imaging, IEEE Access 7 (2019) 164362–164373, https://doi.org/10.1109/ACCESS.2019.2951170.
[6] L. Li, L. Yuan, L. Wang, R. Zheng, Y. Wu, X. Wang, Recent advances in precision measurement & pointing control of spacecraft, Chin. J. Aeronaut. 34 (2021) 191–209, https://doi.org/10.1016/j.cja.2020.11.018.
[7] Y.H. Wu, F. Han, S.J. Zhang, B. Hua, Z.M. Chen, Attitude agile maneuvering control for spacecraft equipped with hybrid actuators, J. Guid. Control Dynam. 41 (2018) 803–812, https://doi.org/10.2514/1.G002982.
[8] R. Geshnizjani, A. Kornienko, T. Ziegler, J. Löhr, W. Fichter, Torque optimal steering of control moment gyroscopes for agile spacecraft, J. Guid. Control Dynam. 44 (2021) 629–640, https://doi.org/10.2514/1.G005118.
[9] N.H. Crisp, P.C.E. Roberts, F. Romano, K.L. Smith, V.T.A. Oiko, V. Sulliotti-Linner, V. Hanessian, G.H. Herdrich, D. García-Almiñana, D. Kataria, S. Seminari, System modelling of very low Earth orbit satellites for Earth observation, Acta Astronaut. 187 (2021) 475–491, https://doi.org/10.1016/j.actaastro.2021.07.004.
[10] X. Wang, G. Wu, L. Xing, W. Pedrycz, Agile earth observation satellite scheduling over 20 Years: formulations, methods, and future directions, IEEE Syst. J. 15 (2020) 3881–3892, https://doi.org/10.1109/jsyst.2020.2997050.
[11] K.Q. Ha, M.D. Femiano, G.E. Mosier, Minimum-time and vibration-avoidance attitude maneuver for spacecraft with torque and momentum limit constraints in redundant reaction wheel configuration, in: L.D. Peterson, R.C. Guyer (Eds.), Space Systems Engineering and Optical Alignment Mechanisms, SPIE, 2004, pp. 126–137, https://doi.org/10.1117/12.558456.
[12] G. Creamer, P. DeLahunt, S. Gates, M. Levenson, Attitude determination and control of Clementine during lunar mapping, J. Guid. Control Dynam. 19 (1996) 505–511, https://doi.org/10.2514/3.21650.
[13] L. You, Y. Dong, Near time-optimal controller based on analytical trajectory planning algorithm for satellite attitude maneuver, Aero. Sci. Technol. 84 (2019) 497–509, https://doi.org/10.1016/j.ast.2018.10.030.
[14] G. Lavezzi, M. Ciarcià, Hybrid open/closed-loop attitude control method for imaging satellites, J. Aero. Eng. 34 (2021), https://doi.org/10.1061/(asce)as.1943-5525.0001293.
[15] G. Lavezzi, M. Ciarcià, A direct method-based suboptimal attitude guidance for accurate ground-target tracking maneuvers, Adv. Space Res. 69 (2022) 3983–4000, https://doi.org/10.1016/j.asr.2022.02.059.
[16] Z. Wang, R. Xu, Rapid search method for a spacecraft attitude maneuver path with multiple constraints, Aero. Sci. Technol. 117 (2021), https://doi.org/10.1016/j.ast.2021.106904, 106904.
[17] J. Han, From PID to active disturbance rejection control, IEEE Trans. Ind. Electron. 56 (2009) 900–906, https://doi.org/10.1109/TIE.2008.2011621.
[18] Y. Hu, B. Wu, Y. Geng, Y. Wu, Smooth time-optimal attitude control of spacecraft, Proc. IME G J. Aero. Eng. 233 (2019) 2331–2343, https://doi.org/10.1177/0954410018776531.
[19] Z. Wang, Y. Yuan, H. Yang, Adaptive fuzzy tracking control for strict-feedback markov jumping nonlinear systems with actuator failures and unmodeled dynamics, IEEE Trans. Cybern. 50 (2020) 126–139, https://doi.org/10.1109/TCYB.2018.2865677.
[20] K. Zhang, S. Wu, Z. Wu, Multibody dynamics and robust attitude control of a MW-level solar power satellite, Aero. Sci. Technol. 111 (2021) 106575, https://doi.org/10.1016/j.ast.2021.106575.
[21] W.A. Wahballah, F. Eltohamy, T.M. Bazan, Influence of attitude parameters on image quality of very high-resolution satellite telescopes, IEEE Trans. Aero. Electron. Syst. 57 (2021) 1177–1183, https://doi.org/10.1109/TAES.2020.3042629.
[22] H. Wang, Z. Yang, Y. Chen, W. Quan, A study on the influence of the satellite attitude accuracy on TDICCD imaging, in: 2012 the 8th IEEE International Symposium on Instrumentation and Control Technology, ISICT 2012 - Proceedings, 2012, pp. 219–223, https://doi.org/10.1109/ISICT.2012.6291634.
[23] W.H. Chen, J. Yang, L. Guo, S. Li, Disturbance-observer-based control and related methods - an overview, IEEE Trans. Ind. Electron. 63 (2016) 1083–1095, https://doi.org/10.1109/TIE.2015.2478397.
[24] S. DIng, W.H. Chen, K. Mei, D.J. Murray-Smith, Disturbance observer design for nonlinear systems represented by input-output models, IEEE Trans. Ind. Electron. 67 (2020) 1222–1232, https://doi.org/10.1109/TIE.2019.2898585.
[25] Y. Zhu, L. Guo, J. Qiao, W. Li, An enhanced anti-disturbance attitude control law for flexible spacecrafts subject to multiple disturbances, Control Eng. Pract. 84 (2019) 274–283, https://doi.org/10.1016/j.conengprac.2018.11.001.
[26] S.I. Addington, C.D. Johnson, Dual-mode disturbance-accommodating pointing controller for hubble space telescope, J. Guid. Control Dynam. 18 (1995) 200–207, https://doi.org/10.2514/3.21370.
[27] Y. Liu, Y. Fu, W. He, Q. Hui, Modeling and observer-based vibration control of a flexible spacecraft with external disturbances, IEEE Trans. Ind. Electron. 66 (2019) 8648–8658, https://doi.org/10.1109/TIE.2018.2884172.
[28] M. Ali, M. Yaqoob, L. Cao, K.H. Loo, Disturbance-observer-based DC-bus voltage control for ripple mitigation and improved dynamic response in two-stage single-phase inverter system, IEEE Trans. Ind. Electron. 66 (2019) 6836–6845, https://doi.org/10.1109/TIE.2018.2879294.
[29] A. Apte, V.A. Joshi, H. Mehta, R. Walambe, Disturbance-observer-based sensorless control of PMSM using integral state feedback controller, IEEE Trans. Power Electron. 35 (2020) 6082–6090, https://doi.org/10.1109/TPEL.2019.2949921.
[30] X. Du, Q. Jin, Modified disturbance observer-based control for stable multivariate processes with multiple time delays, J. Process Control 72 (2018) 52–63, https://doi.org/10.1016/j.jprocont.2018.10.005.
[31] J. Yang, S. Li, X. Chen, Q. Li, Disturbance rejection of dead-time processes using disturbance observer and model predictive control, Chem. Eng. Res. Des. 89 (2011) 125–135, https://doi.org/10.1016/j.cherd.2010.06.006.
[32] F. Zhang, D. Meng, X. Li, Robust adaptive learning for attitude control of rigid bodies with initial alignment errors, Automatica (2021), 110024, https://doi.org/10.1016/j.automatica.2021.110024.
[33] G.F. Franklin, J. Powell, A. Emaminaeini, Pearson, in: Feedback Control of Dynamic Systems, Global Edition, Pearson Schweiz Ag, 2014.
[34] E. Lavretsky, E. Lavretsky, Robust and Adaptive Control : with Aerospace Applications, Springer, 2012.
[35] Z. Wang, J. Yuan, Fuzzy adaptive fault tolerant IGC method for STT missiles with time-varying actuator faults and multisource uncertainties, J. Franklin Inst. 357 (2020) 59–81, https://doi.org/https://doi.org/10.1016/j.jfranklin.2019.09.032.